Nanoscale

Accepted Manuscript

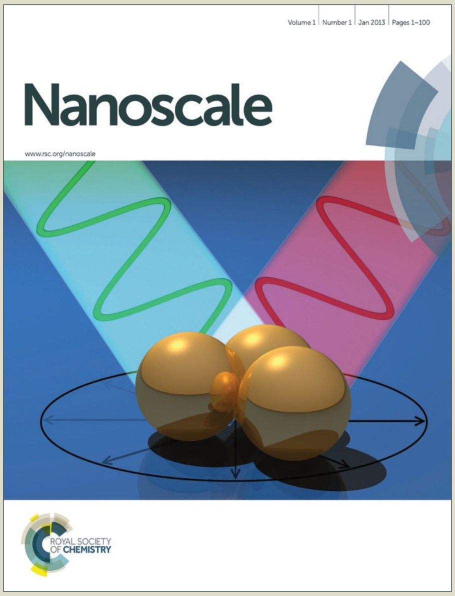

ROYAL SOCIETY OF CHEMISTRY

www.rsc.org/nanoscale

Journal Name

ARTICLE

Theoretical insights into a potential lead-free hybrid perovskite: substituting Pb^{2+} with Ge^{2+}

Received 00th January 20xx,
Accepted 00th January 20xx

DOI: 10.1039/x0xx00000x

www.rsc.org/

Ping-Ping Sun, Quan-Song Li,* Li-Na Yang, Ze-Sheng Li *

In recent years, perovskite solar cells have made considerable development, while the lead in the absorber $MAPbI_3$ is potential threat to the environment. To explore potential alternatives, the structural and electronic properties of MAGeX (X=Cl, Br, I) were investigated by using different density functional theory methods, including GGA-PBE, PBE-SOC, HSE06 and HSE-SOC. The results implied that $MAGeI_3$ exhibits analogous band gap, substantial stability, remarkable optical properties, significant hole and electron conductive behavior compared with the so far widely used absorber MAPbI Moreover, the calculations revealed that the energy splitting resulted from spin-orbit coupling is evident on Pb, moderate on Ge, I and Br, and negligible to Cl. Our work not only sheds some light on screening novel absorbers for perovskite solar cells but also deepens the understanding of these functional materials.

1 Introduction

In the current circumstance, to fully utilize solar energy, perovskite based solar cell has become the rising new star drawing a substantial interest in the field of photovoltaics.[1-9] It has graduated into the most promising alternative to conventional silicon and dye-sensitized solar cells owing to its easy fabrication and high efficiency.[10-12] As of now, the photoconversion efficiency of the best-performing perovskite solar cell as high as 20.2%[8] has been certified by the standardized method in the PV calibration laboratory with a 20.1% efficiency under AM 1.5 G full-sun illuminations,[4, 13] which is comparable to the commercial silicon (20%), CIGS (19.6%), GaAs (18.4%) and CdTe (19.6%) solar cells.[14] The rapid development in perovskite photovoltaic material has attracted increasing attention from both experimental and theoretical aspects,[15-18] however, one of the major issues of perovskite solar cell is that the utilization of lead element can cause serious pollution to the environment. Lead poisoning is toxic to organs and tissues of creatures, damaging nervous and reproductive systems.[19] Thus, the serious environmental complications of lead make it necessary to search for alternative new eco-friendly perovskites before launching them to the public.

Considering the detrimental pollution caused by lead, lead-free perovskites have been developed in order to get comparable or better performance as that of $MAPbI_3$ ($MA=CH_3NH_3$). As the kin element as lead, tin (Sn) has been reported with a great effect, so many attempts have been made to focus on the research of this new material.[20-22] Sn-based perovskites have been reported with an energy gap of about 1.3 eV in both experimental and theoretical results.[23, 2 The analogous $MASnI_3$ perovskite shows a similar structure to $MAPbI_3$ (although in different temperature ranges). Previous reports also indicate that $MASnI_3$ is excellent hole transporter with high mobility and small effective mass.[23, 25] However, for Sn-based perovskites, the main problem is that their efficiency and stability are lower than those of $MAPbI_3$. The Sn-based perovskites are sensitive to the ambient atmosphere with oxygen and moisture, because the instability of $MASnX_3$ (X Br, Cl) is related to the oxidation of Sn^{2+} to Sn^{4+}, which may cause the structure transformation and then bring down the photovoltaic performance.[26] Another viable replacement for Pb is Ge, which belongs to group 14 metals. Compared with $MAPbX_3$ and $MASnX_3$, Ge-based perovskites are less explored in detail. The Ge halide compounds have shown with high ionic conductivity.[27] The similarity between Sn and Ge compounds indicate that the Ge-based perovskite may show analogous solid-state properties to Sn- and Pb-based perovskites.[27, 28] Besides, Ge has also been employed to ABO_3 kind of perovskite and shown excellent electronic and optical properties.[29-31]

A number of computational works have been reported for Pb and Sn-based perovskites,[19, 32-36] however, the detailed systematic theoretical researches on $MAGeX_3$ systems are st temporarily not clear. Recently, the work of Kanatzidis et al. reveals the remarkable optical properties of the Ge-based halide perovskites by replacing the cation A position with small polar organic molecules.[37] This is a breakthrough for the develpomemt of lead-free perovskites. In the present work

---

Key Laboratory of Cluster Science of Ministry of Education, Beijing Key Laboratory of Photoelectronic/Electrophotonic Conversion Materials, School of Chemistry, Beijing Institute of Technology, Beijing 100081, China
E-mail: liquansong@bit.edu.cn; zeshengli@bit.edu.cn.

Electronic Supplementary Information (ESI) available: Optimized structures of $MAPbI_3$ and $MASnI_3$ perovskites, band structures of different perovskite systems shown in different methods, DOS and PDOS structures with different methods of different perovskites, charge density and electrostatic potential plots of different perovskite systems. See DOI: 10.1039/x0xx00000x we systematically study the photovoltaic properties of Ge-based perovskites in trigonal phase (*R3m* space group) versus previous superior halide Pb and Sn-based perovskites with tetragonal phase (*I4/mcm*). Two halogen elements Br and Cl have been substituted on the basis of R3m $MAGeI_3$ model constructing different Ge-based perovskites structures to study their intrinsic properties. The universal models to explain the intrinsic nature of electronic band structures and optical properties about $MAGeX_3$ systems still remain lacking so that the development of the experiment will be impeded. To solve the problem, we explore in detail the roles of s orbital of Ge and p orbitals of halogens in band structures performing with first principle calculations, also with the reason for the high optical absorption coefficients, stability, hole and electron transfer behaviors. We further elucidate the impact of the anti-bonding coupling between s orbital of Ge and p orbitals of X and the high ionicity to better understand the band gap of $MAGeX_3$. Our calculated results suggest that $MAGeI_3$ can be a good absorber to achieve high efficiency as a low cost and good transfer material to apply into the lead-free halide perovskite solar cells.

2 Computational details

All the first-principle calculations are performed by using the Vienna *ab initio* simulation package (VASP).[38] Ion-electron interactions are described with projected augmented wave (PAW) method.[39, 40] A plane wave basis set energy cut-off of 500 eV is employed in the calculation combined with ultrasoft pseudopotentials.[41] Valence configurations include the Pb 5d6s6p, Sn 4d5s5p, Ge 3d4s4p, I 5s5p, Br 4s4p, Cl 3s3p, C 2s2p, N 2s2p and H 1s states. Periodic boundary conditions are applied to all systems. All structures are allowed to relax during the optimization of the geometries with a conjugate-gradient algorithm until the energy on the atoms is less than 1.0×10^{-5} eV. Brillouin-zone integrations use Monkhorst-Pack grids[42] with 6 × 6 × 6 and 8 × 8 × 8 meshes for the calculations of structural optimization and electronic properties, respectively. The generalized gradient approximations (GGA) combining with Perdew-Burke-Ernzerhof (PBE)[43] are used for exchange correlation. Van der Waals (vdW) correction has been verified that it can play an important role in the depiction of perovskite systems with weak interactions,[35] while traditional density functional theory (DFT) with GGA neglects necessary ingredient in the depiction of non-local vdW interactions.[44] Besides, GGA and the local density approximation (LDA) functionals under- or overestimate lattice constants by at least 8%, and it has been found that for perovskites, the variation between the theoretical lattice constants and the experimental data is less than 1% when the non-local vdW functional is employed.[35] Thus, to get a precise theoretical understanding of this weak interactions in hybrid perovskite materials, we optimized all the geometries with vdW correction by using Grimmer's DFT+D2 correction[45] on the basis of GGA-PBE method. It is well known that GGA-PBE gives an underestimated band gap of halide perovskites by canceling the errors with each other in occurrence.[46] Another important issue about perovskite is the spin-orbit coupling (SOC) effect since it is a spin dependent relativistic correction in origin and more prominent for heavy elements such as Pb and Sn.[47] Recently, Even et al. have reported the significant effect of SOC on the band structure of Pb-based perovskites with a reduced band gap by including a large splitting of the first degenerated conduction bands.[48, 49] However, PBE-SOC significantly underestimates the band gap. To correct the band gap underestimation, a screened hybrid functional such as the Heyd-Scuseria-Ernzerhof (HSE06) functional needs to be used and compared to the results of GGA-PBE and PBE-SOC. Furthermore, a more accurate calculation HSE06 combining with SOC (we use HSE-SOC for short) is also used in this work, which is reliable for describing conduction band dispersion.[50] The simulated Pb and Sn-based systems contain four repeated units in the tetragonal phase with lattice parameters a = b = 8.8 Å and c = 12.68 Å for optimization and property calculations.[51, 52] The Ge-based perovskites are taken from the structure synthesised by Kanatzidis et al. with lattice parameters a = b = 8.55 Å and c = 11.16 Å for calculation.[37] Optical properties are determined by the dielectric function $\varepsilon(\omega) = \varepsilon_1(\omega) + i\varepsilon_2(\omega)$ and absorption spectra $A(\omega) = 1\text{-}e^{-\alpha(\omega)\Delta z}$ (Δz is the unit cell size), which are taken from electronic structure. The real part $\varepsilon_1(\omega)$ can be evaluated from imaginary part $\varepsilon_2(\omega)$ using Kramer-Kronig relation, while $\varepsilon_2(\omega)$ can be obtained from the momentum matrix elements between the occupied and unoccupied wave functions.[53, 54] Other optical properties including absorption coefficient $\alpha(\omega)$ = ε2ω/cn(ω), (c is the speed of light in vacuo) and refractivity index $n(\omega)$ can be calculated by $\varepsilon_1(\omega)$ and $\varepsilon_2(\omega)$.[55, 56]

3 Results and discussion

3.1 Structures and formation energies

In order to get a qualitative comprehension of the $MAGeX_3$ structures, their crystallographic stability and probable structures can be deduced by considering a typical useful parameter, the tolerance factor t, introduced by Goldschmidt,[57, 58] which quantifies the structure misfit by treating the ions as packed rigid spheres.[59] For ABX_3 perovskite, t is defined as the ratio of the distance A – X to B – X in the form:

$$t = \frac{1}{\sqrt{2}} \frac{r_A + r_X}{r_B + r_X},$$

where, r_A, r_B, r_X are the ionic radii of corresponding ions. Generally, for halide perovskite, t is in the range of 0.81 ~ 1.11.[60] According to the empirical conditions, a crystal structure can reach an ideal perovskite model when $0.97 < t <$ 1.03.[61] For our systems, A is the organic cation MA^+, generally with r_A = 1.8 Å;[62] X is the halogen anion, where we adopt r_I = 2.2 Å, r_{Br} = 1.96 Å, r_{Cl} = 1.81 Å to get a precise tolerance factor t. Cation B may be Pb with r_B = 1.19 Å, Sn with r_B = 1.1 Å, and Ge with r_B = 0.73 Å. The calculated tolerance factor for $MAPbI_3$, $MASnI_3$, $MAGeI_3$, $MAGeBr_3$, $MAGeCl_3$ crystal structures are 0.834, 0.852, 0.965, 0.988, 1.005, respectively.

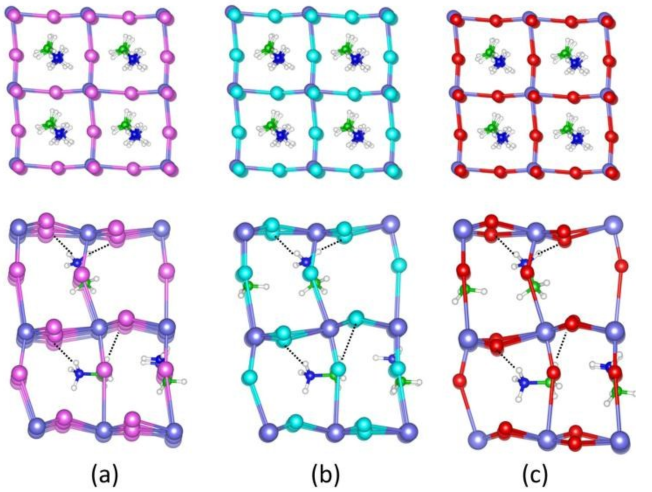

Fig. 1 Optimized stable geometries of (a) $MAGeI_3$, (b) $MAGeBr_3$, (c) $MAGeCl_3$. The upper panel is top view, the under panel is side view. (purple: Ge; pink: I; cyan: Br; red: Cl; green: C; blue: N; white: H) The dash lines are the hydrogen bonds.

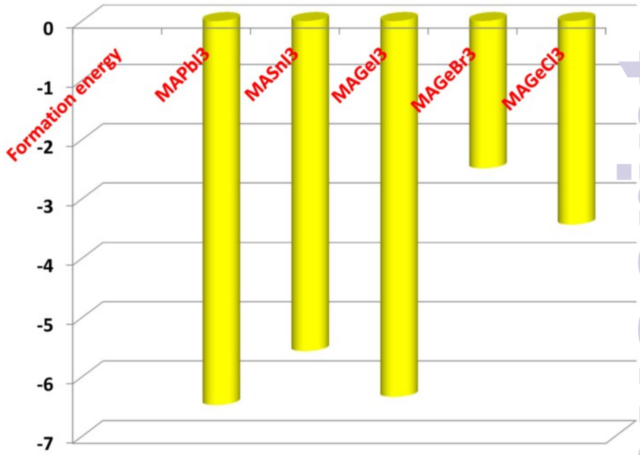

Fig. 2 Calculated formation energy (eV) of the stabl geometries.

Note that, the tolerance factors of Ge containing perovskites are close to that of the empirically ideal perovskite structure.

The optimized stable geometries are shown in Fig. 1 and Fig. S1 (see ESI†). In $MAMI_3$ (M=Pb, Sn, Ge) systems, each metal atom coordinates with six I atoms, where two I atoms in the apical direction and the other four in the equatorial direction with MA^+ filled in the octahedron cages. The optimized configurations of $MAGeX_3$ perovskites as depicted in Fig. 1 exhibit an averaged structure of the distorted geometries, i.e., $Ge - X \cdot\cdot\cdot Ge$ and $Ge \cdot\cdot\cdot X - Ge$. The distortion degree shows a decline trend from chlorine to iodine, and this may be caused by their high ionic conductivity. The optimized lattice constants and available experimental data of $MAMX_3$ are given in Table 1. Apparently, there are big volume contractions going from Pb to Ge, and I to Cl. Specifically, it appears marked lattice constriction change along *a* and *c* directions, that caused by the reduction in atomic radius since both *a* and *c* directions are constructed by the inorganic framework with metal and halogen atoms.

However, in *b* direction, there exists an elongation trend wi the metal atom changes from Pb to Sn, which may be caused by the weak ionic bond interaction between organic cation I ion. Furthermore, the angular values of α, β, γ deviate from 90°, which results from the deformation of the structures. T calculated lattice parameters with DFT+D2 method are in goo agreement with the experimental data provided by Zeng et a with a deviation of 1-2%.[63]

To further explore the equilibrium structures of perovskite the bond lengths and angles of the studied systems are listed in Table 2. The minimum bond length of H_C-X is larger tha that of H_N-X, which indicates that the H_N atom in the cation is more closely located to the M-X chain than that of the H_C atom. The H-N ion shows a more strongly attracted feature to halogen atom by vdW force, because the H-N ion has a large dipole moment than H-C ion. It is obvious that the hydrogen bond between the organic cation and inorganic framework has great effect on the geometry of the investigated systems. Here the hydrogen bond defines as the bond length betwe ammonium hydrogen atoms and halogen atoms with a value less than 2.8 Å. Corresponding hydrogen bonds are displayed in dash lines in Fig.1. Due to the reduction of atomic radius,

Table 1 Calculated lattice parameters for $MAMX_3$ (M=Pb, Sn, Ge; X=I, Br, Cl) perovskites at GGA-D2 level.

Sort	a /Å	b /Å	c /Å	α /°	β /°	γ /°	V/ $Å^3$
$MAPbI_3$	8.89	8.92	13.20	90.06	89.96	90.00	1048.25
$MAPbI_3$ (Exp.)[a]	8.93	8.93	12.67	90	90	90	1011.50
$MASnI_3$	8.73	8.95	12.73	90.05	90.01	89.97	966.15
$MASnI_3$ (Exp.)[a]	8.82	8.82	12.56	90	90	90	977.89
$MAGeI_3$	8.87	8.69	11.53	88.27	91.71	121.55	757.65
$MAGeBr_3$	8.49	8.34	10.92	88.51	91.01	121.53	659.26
$MAGeCl_3$	8.42	8.07	10.42	88.44	91.17	122.63	596.06

[a] From Ref. [63].

Table 2 Calculated range of bond lengths and bond angles for $MAMX_3$ (M=Pb, Sn, Ge; X=I, Br, Cl) systems with GGA-D2 method.

sort	$MAPbI_3$	$MASnI_3$	$MAGeI_3$	$MAGeBr_3$	$MAGeCl_3$
H_N-X/Å	2.61-3.62	2.61-3.53	2.65-3.54	2.39-3.41	2.22-3.57
H_C-X/Å	3.11-3.37	3.23-3.46	3.25-3.65	3.17-3.63	2.95-3.31
M-X1(equatorial) /Å	3.20-3.28	2.82-3.64	2.71-3.65	2.52-3.65	2.35-3.66
M-X2(apical) /Å	3.22-3.40	2.82-3.63	2.76-3.43	2.53-3.69	2.36-3.68
M-X-M(equatorial)/deg	151-154	153-167	151-169	152-171	152-167
M-X-M(apical)/deg	171-172	167-168	162-165	160-168	155-169

the bond lengths of M-X in both equatorial and apical directions present a similar trend to the lattice parameters. Both bond lengths and angles of M-X are greatly affected by the distribution of MA^+. The experimental data of the average Pb-I and Sn-I bond lengths are 3.16 Å and 3.13 Å, respectively.[23] The bond length ranges listed in Table 2 about $MAPbI_3$ and $MASnI_3$ reproduce the long-short alternation tendency of the M-I bonds.[23] Compared to Pb- and Sn-based perovskites, the bond lengths and angles of $MAGeX_3$ show a similar degree of deformation characteristics.

The bottle-neck for the development of perovskite solar cells is the stability of $MAMX_3$, which can be estimated by the formation energy. Based on the UV-vis spectra and X-ray photoelectron spectroscopy results, the formation process of perovskite can be expressed as follows:

$$MAX + MX_2 \rightarrow MAMX_3$$

where X represents I, Br and Cl, M stands for Pb, Sn and Ge elements. In order to simplify the free energy of the above equation, we define the formation energy of perovskites with the following equation, as shown below:

$$E_f = E(MAMX_3) - E(MAX) - E(MX_2)$$

where E_f is the formation energy, $E(MAMX_3)$, $E(MAX)$ and $E(MX_2)$ are the corresponding total energy obtained from DFT+D2 calculations. The calculated formation energies of the perovskites are shown in Fig. 2. According to the definition above, a negative E_f corresponds to a stable geometry, and the more negative, the more stable. So the stability order of the five perovskites is $MAPbI_3$ > $MAGeI_3$ > $MASnI_3$ > $MAGeCl_3$ > $MAGeBr_3$. Particularly, $MAGeI_3$ and $MAPbI_3$ have little difference in the value of formation energy, indicating that $MAGeI_3$ has the similar stability with $MAPbI_3$. Recently, Li *et al.* reported that montmorillonite can act as bifunctional buffer layer to limit charge recombination and protect perovskite from corrosion,[64] so montmorillonite can be used for $MAGeI_3$ perovskite to improve its stability.

Based on the analysis of the structural properties and formation energies of the five systems, it is clear that weak interactions between the cation MA^+ and the inorganic framework have an important effect on determining the equilibrium structures and stability of perovskite.

3.2 Electronic properties

The band gap is an important factor on determining many physical properties such as the absorption, photoconductivity and electroluminescence. The calculated direct band gaps of $MAMX_3$ at the Γ point of the Brillouin zone with different methods are presented in Table 3. The band structures of $MAMX_3$ are displayed in Fig. S2-S5. The band gap of $MAPbI_3$ with PBE method is 1.53 eV, which matches well with previous theoretical result of 1.63 eV[46] and is among the experimental range of 1.5-1.67 eV.[3, 65, 66] Besides, the band gap of $MASnI_3$ with PBE functionals is 0.61 eV, in good agreement with the previous theoretical result of 0.61 eV.[34] Among the three Ge-based perovskites, the band gap of $MAGeI_3$ with PBE functional 1.61 eV matches well with that of $MAPbI_3$ (E_{exp}=1.55 eV), while the band gaps of $MAGeBr_3$ (2.81 eV) and $MAGeCl_3$ (3.76 eV) are much larger. So in terms of band matching, $MAGeI_3$ is superior to the other two Ge-based perovskites.

Besides, DFT+D2, vdW-DF2 and optB88-vdW approaches have also been employed to deal with the van der Waals interactions. The band gaps of $MAPbI_3$ and $MAGeI_3$ are 1.92 eV and 1.96 eV by vdW-DF2, and 2.04 eV and 2.05 eV by

Table 3 Calculated band gaps of $MAMX_3$ structures with different DFT methods. The experimental results are listed in parallel.

Phase/eV	PBE	PBE-SOC	HSE06	HSE-SOC	Exp.
$MAPbI_3$	1.53	0.63	2.02	1.05	1.5^a-1.66^b
$MASnI_3$	0.61	0.37	1.57		1.1^a-1.3^c
$MAGeI_3$	1.61	1.48	2.16	2.04	1.9^d
$MAGeBr_3$	2.81	2.76			
$MAGeCl_3$	3.76	3.74			

[a] from Ref. [3]; [b] from Ref.[46] ; [c] from Ref.[34] , [d] from Ref.[37].

optB88-vdW. Clearly, the vdW-DF2 and optB88-vdW treatments overestimate the band gaps compared with DFT-D2 method with respect to the experimental data. As for the spin-orbit coupling effects, the SOC shows a dramatic effect on the conduction band region with a sharp reduction of the bottom of the conduction band. This reduction is caused by the splitting of the conduction band into two-fold degenerate state |1/2, ±1/2> corresponding to light electrons and four-fold degenerate states |3/2, ±3/2>, |3/2, ±1/2> corresponding to heavy electrons at the Γ point.[67] It follows that the band gap reduced to 0.63 eV for $MAPbI_3$ and 0.37 eV for $MASnI_3$, which are much lower than the experimental data of 1.55 eV[1] and 1.2 eV,[34] respectively. While the band gaps with SOC of the three Ge-based perovskites are 1.48 eV ($MAGeI_3$), 2.76 eV ($MAGeBr_3$), and 3.74 eV ($MAGeCl_3$), which are lower than the results without SOC effect by only 0.13 eV, 0.05 eV and 0.02 eV. This means the SOC has a rather weak energy splitting effect on the band structure of Ge-based perovskites. Comparing Fig. S2 (b) and Fig. S3 (b), the SOC shows a dramatic effect on the conduction band region with a sharp reduction of the bottom of the conduction band for $MAPbI_3$ and $MASnI_3$, while the energy splitting on the CBM of the three Ge-based perovskites is much weaker. It can be clearly seen from Fig. S4 (b) and Fig. S5 that the bands of CBM and CBM+1 (we define the first and the second band from the bottom of conduction bands as CBM and CBM+1) begin to split into two bands along the Z to Γ direction, but both bands overlap again in the region near F point. However, for the band of $MAPbI_3$ with SOC effect (see Fig. S2 (b)), both CBM and CBM+1 keep two isolated bands along the Γ to F direction after energy splitting. The same case also happens in the SOC-band structure of $MAGeBr_3$, while this phenomenon cannot be found in the SOC-band structure of $MAGeCl_3$, where the CBM still keeps a single line after the influence of the SOC effect. It can be speculated that SOC has such a weak effect not only on Ge, but also on the halogen atoms I and Br, and there is negligible effect on Cl atom.

However, it is well known that GGA-PBE and PBE-SOC underestimate the band gaps of halide perovskites. Comparing with GGA-PBE and PBE-SOC results of the five perovskites, it is obvious that $MAGeI_3$ compared well with $MAPbI_3$, while both $MAGeBr_3$ and $MAGeCl_3$ show wide band gaps which may be unsuitable for the perovksite application. In order to obtain more accurate band gaps, we adopt HSE06 and HSE-SOC calculations. However, both HSE06 and HSE-SOC calculations are quite time-consuming. Considering the calculation cost, we adopt HSE06 for $MAPbI_3$, $MASnI_3$ and $MAGeI_3$. The results of band gaps calculated by HSE06 shown in Table 3 and Fig. S2-S4 (c) are larger than the relevant experimental data mainly due to the lift of the conduction band energies. To further explore the band gaps of $MAPbI_3$ and $MAGeI_3$, a higher precision calculation HSE-SOC is used here, only for $MAPbI_3$ and $MAGeI_3$ to analyze the correlation between the two preferably. The combination of HSE06 and SOC can give an accurate result by push-pull energy counteraction, one raising up the conduction band and the other pulling down the same object with strong energy splitting. The result of $MAPbI_3$ calculated by HSE-SOC shows a slightly lower band gap compared with its experimental value, while the result of $MAGeI_3$ is almost equal to its experimental data. This phenomenon turns out that Pb has a stronger SOC effect than Ge, which pulls down the CBM energy, while Ge gives a small SOC effect signal to HSE-SOC method, that leads to the result close to the experimental value.

To further understand the electronic structures of the five perovskites, the density of states are analyzed. The DOS structures with and without SOC on the basis of GGA+D2 calculation are shown in Fig. 3, and the DOS with other calculation methods are shown in the ESI† (Fig. S6-S9). The DOS of each kind of perovskites with the five calculation methods gives a similar component curve. DOS with HSE06 and HSE-SOC calculations give a more acute and intensive volatility. From the projected density of states (PDOS) in Fig. S6-S9, it is clear that the GGA+D2 correction has a greater effect on the orbital contribution than SOC effect, reflected in both PBE-SOC and HSE-SOC DOS structures, because the peak intensities of their PDOS with SOC effect are very weak, which can be hardly seen in Fig. 3. Comparing the total density of states (TDOS) of $MAPbI_3$ and $MASnI_3$ structures, a shift of SOC TDOS has been reflected in the region near zero point showing a shrunken band gap. This phenomenon is more obvious in $MAPbI_3$, where both valence bands and conduction bands have a shift toward zero point. This can be interpreted that Pb atom has a larger spin-orbit coupling constant than that of Sn atom. Both structures have two peaks in the valence band maximum (VBM) and the peak intensities are weaker than that of TDOS with GGA+D2 calculation. We consider that SOC may also give rise to a weak energy splitting to the VBM. As shown in Fig. 3, the main contribution to VBM is from the 5p orbitals of I atom with an overlap of s orbitals of Pb and Sn atoms, while the CBM is dominated by p orbitals of Pb and Sn atoms, partly hybridized with I orbitals. Besides, the MA^+ cations have also a weak contribution to the CBM and VBM around the Fermi energy level (E_{Fermi} has been adjusted to zero point).

As for TDOS of the three Ge-based perovskites, the SOC results show a weak shift on the CBM and VBM edges in both $MAGeI_3$ and $MAGeBr_3$. The peak splitting on valence bands of $MAGeI_3$ is similar to those of Pb- and Sn-based systems, while for $MAGeBr_3$, it only shows weaker peak intensity change and without peak splitting in valence bands. However, the SOC TDOS of $MAGeCl_3$ shows a complete overlap to the TDOS without SOC correction. This means that SOC has a weak energy splitting on the valence bands, which also confirms the conclusion drawn from $MAPbI_3$ and $MASnI_3$ results. Besides, SOC has a weaker energy splitting effect on Ge atom than that of Pb and Sn atoms reflected on the band gap change. More importantly, the different degrees of peak splitting in the valence bands also indicate that that SOC has some effects on I and Br atoms since I and Br are heavy atoms in the same periodic with Sn and Ge, separately, but there is a negligible SOC effect on Cl atom. Similar to the PDOS of $MAPbI_3$ and $MASnI_3$, the SOC-PDOS of the three Ge-based perovskites show weak intensity as shown in Fig. S8-S9, which are less

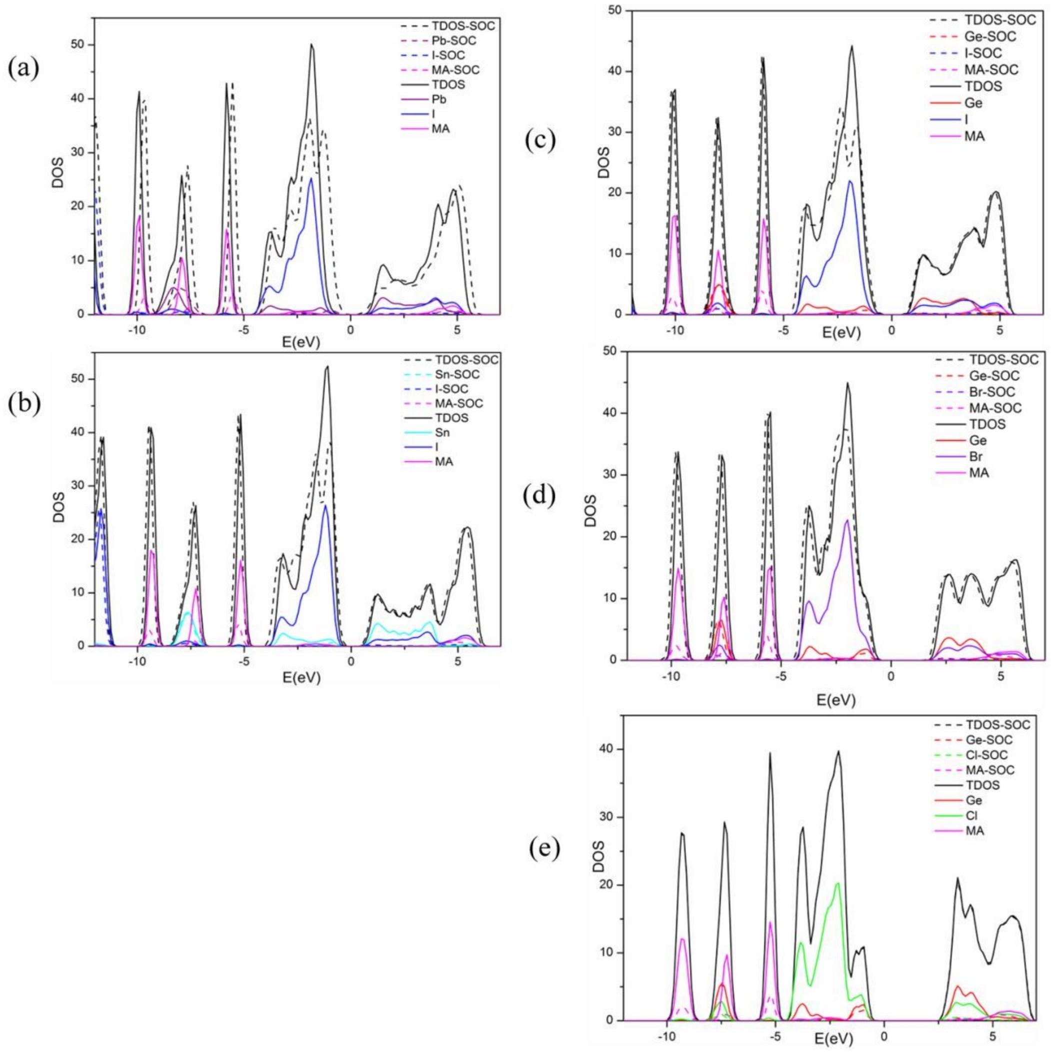

Fig. 3 DOS structure of (a) MAPbI$_3$, (b) MASnI$_3$, (c) MAGeI$_3$, (d) MAGeBr$_3$, (e) MAGeCl$_3$. The dash and solid lines represent the results calculated with and without SOC effect, respectively.

dramatic curves in Fig. 3 (c)-(e). The main contributions to VBM of the three Ge-based perovskites are from the p orbitals of halogens with an overlap of s orbital of Ge, while CBM is dominated by p orbitals of Ge atom. Besides, the MA$^+$ cations also have a weak contribution to the conduction bands and valence bands. These features can be seen in the charge densities of the CBM and VBM shown in the middle and right panel of Fig. 4 (a). We take MAGeI$_3$ for example with more details. The yellow isosurfaces in the VBM are distributed on 5p orbials of I and 4s orbital of Ge, while in the CBM, are with 4p orbitals of Ge. It means that electrons distribute around the CBM and holes are around the VBM, respectively. Such results manifest that the electrons and holes can separate effectively between CBM and VBM, since the electrons on the 5p orbitals of I and 4s orbital of Ge are excited to 4p orbitals of Ge under photo excitation.

Furthermore, both the total charge density shown in the left panel of Fig. 4 (a) and the PDOS in Fig. 3 indicate that MA$^+$ cation does not directly donate electronic states to the band edges (both CBM and VBM), which affects the inorganic framework mediately by weak interactions. It is clear that the charge accumulates in the region between I atoms and MA$^+$ matrix which confirms the formation of H-I hydrogen bond. The similar situation also exists in MAPbI$_3$, MASnI$_3$, MAGeBr$_3$ and MAGeCl$_3$, as shown in Fig. S10. To gain a deeper understanding of the coupling between MA$^+$ and Ge-I chains, contour plots of electrostatic potential are drawn in specific surface as shown in Fig. 4 (b). The coupling is quite weak since there is no electron orbital overlap between the cation MA$^+$ and I atoms. It means that there is a strong ionic nature between the organic molecule and I atoms. But there are strong overlap between Ge and I atoms which means that there are strong covalent bonding in the Ge-I chains. Especially, the weak contour lines between H and I also indicate that a weak interaction exists between the two types of atoms forming H-I hydrogen bond. In the electrostatic potential of VBM, it is mainly the anti-bonding component of the hybridization between s orbital of Ge and p orbitals of I, wh

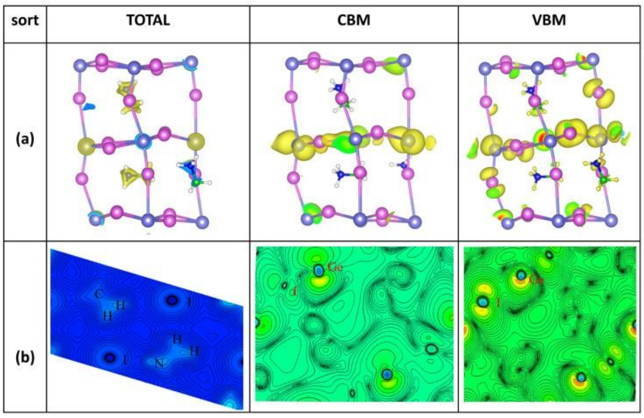

Fig. 4 (a) Charge density of $MAGeI_3$, the left panel is total charge density, the middle panel is CBM charge density, the right panel is VBM charge density; (b) electrostatic potential of $MAGeI_3$, the left panel is total electrostatic potential of (101) surface, the middle panel is CBM electrostatic potential of (110) surface, the right panel is VBM electrostatic potential of (110) surface.

the CBM is almost a non-bonding state dominated by the p orbitals of Ge. The same covalent and ionic natures can also be found in $MAPbI_3$, $MASnI_3$, $MAGeBr_3$ and $MAGeCl_3$, as shown in Fig. S11.

To get more insight into the electron distribution on the bands near the VBMs and CBMs of $MAGeI_3$, the band structure and parial orbital charge densities of VBM-1, VBM-2, VBM-3, CBM+1, CBM+2, CBM+3 bands are displayed in Fig. 5. The electron densities of VBM (Fig. 4), VBM-1, VBM-2, VBM-3 are primary located on Ge and I atoms, and its electron density increases as the valence band rises. The densities from CBM (Fig. 4) to CBM+3 accumulate around the p orbitals of Ge atoms with little difference as the band energy change, which indicate that the electrons leap from the valence bands to conduction bands, gathering the holes with VBMs. As for the proper band gap between CBM and VBM, it promotes the electrons to inject into the conduction bands, thus raising the photovoltaic efficiency.

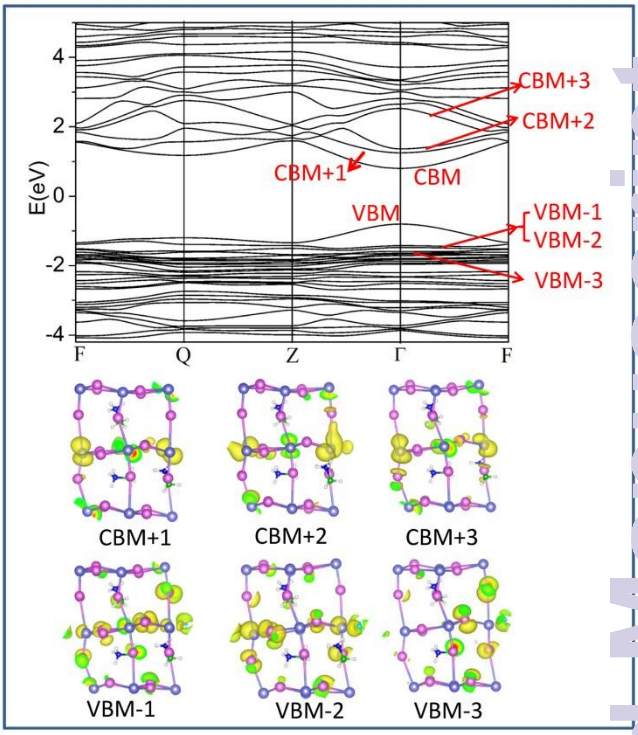

Fig. 5 Partial orbital charge densities of $MAGeI_3$ of some CBMs and VBMs bands corresponding to the relevant band structure.

Since the photo-generated electrons and holes in perovskite thermally relax to the CBM and VBM, respectively, a sma effective mass can facilitate the transportation of the electrons and holes. Their effective masses (m_e* and m_h*) are calculate via the following equation

$$m^* = \hbar^2 \left[\frac{\partial^2 \mathcal{E}(k)}{\partial k^2}\right]^{-1}$$

where $\mathcal{E}(k)$ is the band edge eigenvalues, k is the wavevecto Since different calculation methods give different band structures, which can lead to the band dispersion change alo the high symmetry directions of the Brillouin zone as the band

Table 4 Effective mass m* and the corresponding reduced masses μ for the researched systems in Γ-F direction.

sort		$MAPbI_3$	$MASnI_3$	$MAGeI_3$	$MAGeBr_3$	$MAGeCl_3$
PBE	m_e*/m_0	0.321	0.420	0.316	0.691	0.347
	m_h*/m_0	0.481	0.412	0.412	0.522	0.408
	μ	0.192	0.208	0.178	0.297	0.187
PBE-SOC	m_e*/m_0	0.279	0.393	0.214	0.448	0.232
	m_h*/m_0	0.271	0.235	0.209	0.276	0.281
	μ	0.137	0.147	0.106	0.171	0.127
HSE06	m_e*/m_0	0.111	0.323	0.211		
	m_h*/m_0	0.203	0.176	0.174		
	μ	0.072	0.114	0.095		
HSE-SOC	m_e*/m_0	0. 073		0.168		
	m_h*/m_0	0.077		0.117		
	μ	0.037		0.069		

gap change aforementioned. As well this also leads to sizable differences for the calculated effective masses of electrons and holes, derived by parabolic band fitting around the Γ to F direction of the Brillouin zone. These effective masses (Γ to F direction) are listed in Table 4, and effective masses in F-Q, Q-Z, Z-Γ directions are listed in Table S1 and Table S2. We also compare the calculated reduced masses $\mu = m_e \cdot m_h / (m_e + m_h)$ with experimental data for $MAPbI_3$ with a range of 0.09 – 0.15 m_0 (m_0 is the electron static mass).[68] The calculated μ values with different methods for the five objects are matchable with the experimental values range. In actual crystal, there exist several elastic scatterings caused by photons and structural defects and impurities which would increase the effective masses, so the estimated effective masses are obtained with minimizing these scatterings in perovskites crystals.[67] It can be seen that these electron effective masses are slightly higher than those of the measured semiconductors used in photovoltaic cells, and the hole effective masses are smaller than those of similar semiconductors.[33] The effective masses act out a decline trend with the improvement of the calculation method as shown in Table 4. The effective masses of $MAPbI_3$ and $MASnI_3$ with PBE-SOC and HSE06 methods agree well with previous publications.[34, 48, 69] For the three Ge-based perovskites, their effective masses show comparable property to those of $MAPbI_3$ and $MASnI_3$. Thus, $MAGeCl_3$ may be a good electron transporter with relative small m_e* value, and $MAGeBr_3$ probably demonstrates a mediocre transport ability. In terms of $MAGeI_3$, broadly speaking, it shows more excellent electron and hole transport nature than both $MAPbI_3$ and $MASnI_3$ under similar conditions, so it can be considered as a good choice to substitute $MAPbI_3$.

3.3 Optical properties

To probe the light absorption ability of five perovskites $MAPbI_3$, $MASnI_3$, $MAGeI_3$, $MAGeBr_3$ and $MAGeCl_3$ in the visible zone, the optical absorption coefficients of the five structures are obtained and shown in Fig. 6 (a). Recently, Feng et al.[63] have calculated the absorption spectra of $MAPbI_3$ and $MASnI_3$ with TDDFT method. The absorption of $MAPbI_3$ and $MASnI_3$ in our work agrees well with their results. $MASnI_3$ shows the strongest absorption in the entire visible solar spectrum, and the spectrum of $MAPbI_3$ shows a blue shift with respect to $MASnI_3$. In the whole visible region (380 nm to 780 nm) $MAGeI_3$ shows a comparable absorption ability with $MAPbI_3$. Unlike $MAPbI_3$, $MAGeI_3$ has a weak absorption in the ultraviolet spectrum. Such results also agree with the trend of band gap discussed above. For the absorption spectrum of three Ge-based perovskites in the visible light region, $MAGeI_3$ with a large red shift and coefficient is better than $MAGeBr_3$ and $MAGeCl_3$, while Br and Cl-based perovskites only respond strongly to the ultraviolet spectrum. Besides, according to the absorption spectra of $MAGeI_3$ in Ref. 37, it has the absorption in 1.9-3.6 eV, namely, in 350-650 nm spectrum region, which shows the same trend with our results. The absorption of $MAGeI_3$ is in good agreement with the experimental result. For further study of solar energy harvesting property, we calculate the dielectric function of the five perovskites. The real and imaginary parts of the dielectric function are shown in Fig. 6 (b). For the computed structures, their dielectric spectra in the imaginary parts demonstrate two peaks below 500 nm, and then show downward trend. Among the five imaginary parts, the computed intensities of $MASnI_3$ are higher than the other structures, which corresponds to the biggest absorption coefficient as displayed in Fig. 6 (a). For the real parts, the absorption near 180 nm becomes negative, which means that they have strong absorption in the ultraviolet spectrum. The second absorption can be seen in the range of 300-400 nm in the calculated dielectric spectra. This absorption is basically located at the near ultraviolet spectrum. From the calculated dielectric spectra, $MAGeI_3$ has a good overlap with $MAPbI_3$ both on the imaginary and real parts. So $MAGeI_3$ exhibits good solar energy absorption ability in the visible light spectrum.

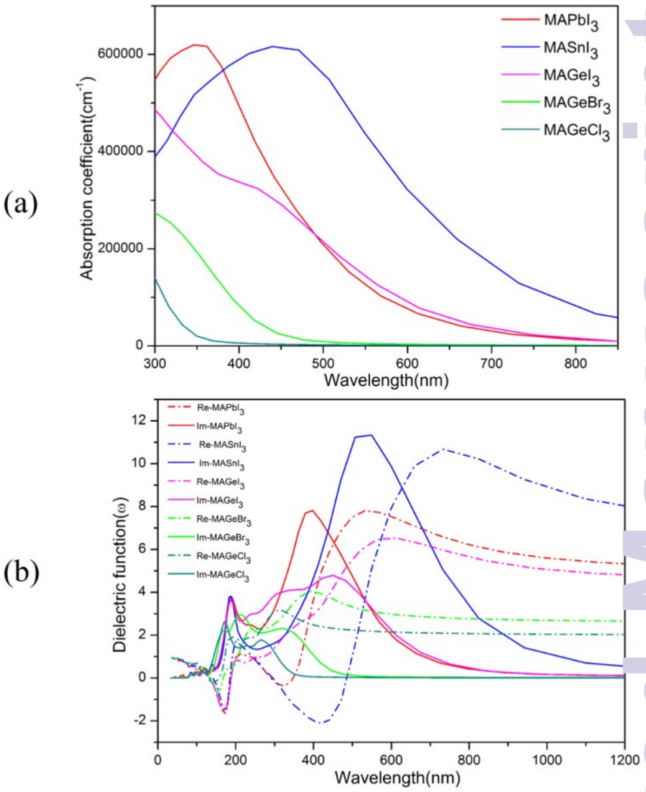

Fig. 6 Calculated (a) absorption spectra and (b) dielectric spectra of $MAMX_3$ systems. In the dielectric spectra, the imaginary parts are shown in solid lines, and the real parts are shown in dash lines.

4 Conclusions

In this paper, we report the calculations with spin-orbit coupling (SOC) effect and combining with high-precision hybrid functional (HSE06) calculation HSE-SOC to analyze the structural, electronic and optical properties of $MAMX_3$ ($MA=CH_3NH_3$; M=Pb, Sn, Ge; X=I, Br, Cl) perovskites. The obtained results reveal that unlike the evident SOC effect

Pb-containing system, the energy splitting of SOC effect in valence band and conduction band is moderate on Ge, I and Br, but almost negligible to Cl. The more accurate calculations of HSE06 and HSE-SOC further turn out that $MAGeI_3$ exhibits a electronic character which can be on a par with $MAPbI_3$. Compared with Sn-based perovskites, where $MASnI_3$ is sensitive to oxygen and moisture, easily oxidized from Sn^{2+} to Sn^{4+}, thus brings down the photovoltaic performance. The Ge analogues differ from their heavier congeners because they show a pronounced tendency to crystallize in polar space group. This behavior of Ge iodides has been confirmed by patent application.[37] Furthermore, the effective masses and the formation energies illustrate that $MAGeI_3$ has a remarkable hole and electron conductive behavior and adequate stability compared with $MAPbI_3$. The optical properties of $MAGeI_3$ present a similar absorption ability with $MAPbI_3$. All these results suggest that $MAGeI_3$ may be a competitive and environmental friendly alternative to $MAPbI_3$ for efficient perovskite solar cells.

Acknowledgements

The authors gratefully acknowledge financial support from the Major State Basic Research Development Programs of China (2011CBA00701), the National Natural Science Foundation of China (21473010, 21303007).

Notes and references

1 A. Kojima, K. Teshima, Y. Shirai and T. Miyasaka, *J. Am. Chem. Soc.*, 2009, **131**, 6050-6051.
2 G. E. Eperon, S. D. Stranks, C. Menelaou, M. B. Johnston, L. M. Herz and H. J. Snaith, *Energy Environ. Sci.*, 2014, **7**, 982-988.
3 F. Hao, C. C. Stoumpos, R. P. H. Chang and M. G. Kanatzidis, *J. Am. Chem. Soc.*, 2014, **136**, 8094-8099.
4 H. Zhou, Q. Chen, G. Li, S. Luo, T. b. Song, H. S. Duan, Z. Hong, J. You, Y. Liu and Y. Yang, *Science*, 2014, **345**, 542-546.
5 W. J. Chi, Q. S. Li and Z. S. Li, *J. Phys. Chem. C*, 2015, **119**, 8584-8590.
6 W. J. Chi and Z. S. Li, *Phys. Chem. Chem. Phys.*, 2015, **17**, 5991-5998.
7 N. J. Jeon, J. H. Noh, W. S. Yang, Y. C. Kim, S. Ryu, J. Seo and S. I. Seok, *Nature*, 2015, **517**, 476-480.
8 W. S. Yang, J. H. Noh, N. J. Jeon, Y. C. Kim, S. Ryu, J. Seo and S. I. Seok, *Science*, 2015, **348**, 1234-1237.
9 M. F. Xu, H. Zhang, S. Zhang, H. L. Zhu, H. M. Su, J. Liu, K. S. Wong, L. S. Liao and W. C. H. Choy, *J. Mater. Chem. A*, 2015, **3**, 14424-14430.
10 J. Cao, J. Yin, S. Yuan, Y. Zhao, J. Li and N. Zheng, *Nanoscale*, 2015, **7**, 9443-9447.
11 T. Liu, D. Kim, H. Han, A. R. b. Mohd Yusoff and J. Jang, *Nanoscale*, 2015, **7**, 10708-10718.
12 C. Ying, C. Shi, N. Wu, J. Zhang and M. Wang, *Nanoscale*, 2015, **7**, 12092-12095.
13 http://www.nrel.gov/ncpv/images/efficiency_chart.jpg, 2015.
14 M. A. Green, K. Emery, Y. Hishikawa, W. Warta and E. D. Dunlop, *Prog. Photovolt: Res.Appl.*, 2014, **22**, 701-710.
15 E. Mosconi, P. Umari and F. De Angelis, *J. Mater. Chem. A*, 2015, **3**, 9208-9215.
16 J. Navas, A. Sanchez-Coronilla, J. J. Gallardo, N. Cruz Hernandez, J. C. Pinero, R. Alcantara, C. Fernandez-Lorenzo, D. M. De los Santos, T. Aguilar and J. Martin-Calleja, *Nanoscale*, 2015, **7**, 6216-6229.
17 J. Xi, Z. Wu, H. Dong, B. Xia, F. Yuan, B. Jiao, L. Xiao, Q. Gong and X. Hou, *Nanoscale*, 2015, **7**, 10699-10707.
18 C. Quarti, E. Mosconi and F. De Angelis, *Chem. Mater.*, 2014, **26**, 6557-6569.
19 J. Feng and B. Xiao, *J. Phys. Chem. C*, 2014, **118**, 19655-19660.
20 F. Hao, C. C. Stoumpos, D. H. Cao, R. P. H. Chang and M. G. Kanatzidis, *Nat Photon*, 2014, **8**, 489-494.
21 N. K. Noel, S. D. Stranks, A. Abate, C. Wehrenfennig, S. Guarnera, A. A. Haghighirad, A. Sadhanala, G. E. Eperon, S. K. Pathak, M. B. Johnston, A. Petrozza, L. M. Herz and H. J. Snaith, *Energy Environ. Sci.*, 2014, **7**, 3061-3068.
22 B. Wang, X. Xiao and T. Chen, *Nanoscale*, 2014, **6**, 12287-12297.
23 C. C. Stoumpos, C. D. Malliakas and M. G. Kanatzidis, *Inorg. Chem.*, 2013, **52**, 9019-9038.
24 E. M. Paolo Umari, Filippo De Angelis, *Sci. Rep.*, 2013, 4, 4467.
25 I. Chung, B. Lee, J. He, R. P. H. Chang and M. G. Kanatzidis, *Nature*, 2012, **485**, 486-489.
26 Z. Xiao, H. Lei, X. Zhang, Y. Zhou, H. Hosono and T. Kamiya, *B. Chem. Soc. Jpn.*, 2015, DOI: 10.1246/BCSJ.20150110.
27 K. Yamada, K. Isobe, E. Tsuyama, T. Okuda and Y. Furukawa, *Naturforsch*, 1994, **49a**, 258-266.
28 S. J. Clark, J. D. Donaldson and J. A. Harvey, *J. Mater. Chem.*, 1995, **5**, 1813-1818.
29 C. A. Barboza, J. M. Henriques, E. L. Albuquerque, E. W. S. Caetano, V. N. Freire and J. A. P. da Costa, *Chem. Phys. Lett.*, 2009, **480**, 273-277.
30 H. R. Fuh, Y. P. Liu, S. H. Chen and Y. K. Wang, *J. Alloy Compd.*, 2013, **547**, 126-131.
31 M. F. M. Taib, M. K. Yaakob, F. W. Badrudin, M. S. A. Rasiman, T. I. T. Kudin, O. H. Hassan and M. Z. A. Yahya, *Integr. Ferroelectr.*, 2014, **155**, 23-32.
32 Y. He and G. Galli, *Chem. Mater.*, 2014, **26**, 5394-5400.
33 E. Menéndez-Proupin, P. Palacios, P. Wahnón and J. C. Conesa, *Phys. Rev. B*, 2014, **90**, 045207.
34 P. Umari, E. Mosconi and F. De Angelis, *Sci. Rep.*, 2014, 4, 4467.
35 Y. Wang, T. Gould, J. F. Dobson, H. Zhang, H. Yang, X. Yao and H. Zhao, *Phys. Chem. Chem. Phys.*, 2014, **16**, 1424-1429.
36 Y. Wang, B. G. Sumpter, J. Huang, H. Zhang, P. Liu, H. Yang and H. Zhao, *J. Phys. Chem. C*, 2014, **119**, 1136-1145.
37 C. C. Stoumpos, L. Frazer, D. J. Clark, Y. S. Kim, S. H. Rhim, A. J. Freeman, J. B. Ketterson, J. I. Jang and M. G. Kanatzidis, *J. Am. Chem. Soc.*, 2015, **137**, 6804-6819.
38 G. Kresse and J. Furthmuller, *Phys. Rev. B*, 1996, **54**, 11169-11186.
39 P. E. Blöchl, *Phys. Rev. B*, 1994, **50**, 17953-17979.
40 G. Kresse and D. Joubert, *Phys. Rev. B*, 1999, **59**, 1758-1775.
41 D. Vanderbilt, *Phys. Rev. B*, 1990, **41**, 7892-7895.
42 H. J. Monkhorst and J. D. Pack, *Phys. Rev. B*, 1976, **13**, 5188-5192.
43 J. P. Perdew, K. Burke and M. Ernzerhof, *Phys. Rev. Lett.*, 1996, **77**, 3865-3868.
44 Y. Andersson, D. C. Langreth and B. I. Lundqvist, *Phys. Rev. Lett.*, 1996, **76**, 102-105.
45 S. Grimme, *J. Comput. Chem.*, 2006, **27**, 1787-1799.
46 E. Mosconi, A. Amat, M. K. Nazeeruddin, M. Grätzel and F. De Angelis, *J. Phys. Chem. C*, 2013, **117**, 13902-13913.
47 F. Neese, *J. Chem. Phys.*, 2005, **122**, 034107.
48 J. Even, L. Pedesseau, J. M. Jancu and C. Katan, *J. Phys. Chem. Lett.*, 2013, **4**, 2999-3005.
49 J. Even, L. Pedesseau, M. A. Dupertuis, J. M. Jancu and C. Katan, *Phys. Rev. B*, 2012, **86**, 205301.
50 J. Heyd, G. E. Scuseria and M. Ernzerhof, *J. Chem. Phys.*, 2003, **118**, 8207-8215.

51 A. Poglitsch and D. Weber, *J. Chem. Phys.*, 1987, **87**, 6373-6378.

52 Y. Kawamura, H. Mashiyama and K. Hasebe, *J. Phys. Soc. Jpn.*, 2002, **71**, 1694-1697.

53 J. H. Luo, Q. Liu, L. N. Yang, Z. Z. Sun and Z. S. Li, *Comp. Mater. Sci.*, 2014, **82**, 70-75.

54 M. C. P.Y. Yu, *Phys. Today*, 1997, **50**, 76.

55 S. Saha, T. P. Sinha and A. Mookerjee, *Phys. Rev. B*, 2000, **62**, 8828-8834.

56 M. Cazzaniga, L. Caramella, N. Manini and G. Onida, *Phys. Rev. B*, 2010, **82**, 035104.

57 V. M. Goldschmidt, *Naturwissenschaften*, 1926, **15**, 477-485.

58 V. M. Goldschmidt, *Ber. dtsch. chem. Ges. (A and B Series)*, 1927, **60**, 1263-1296.

59 A. Filippetti and A. Mattoni, *Phys. Rev. B*, 2014, **89**, 125203.

60 M. A. Green, A. Ho-Baillie and H. J. Snaith, *Nat Photon*, 2014, **8**, 506-514.

61 L. C. Tang, Y. C. Chang, J. Y. Huang, M. H. Lee and C. S. Chang, *Jpn. J. Appl. Phys.*, 2009, **48**, 112402.

62 N. K. McKinnon, D. C. Reeves and M. H. Akabas, *J. Gen. Physiol.*, 2011, **138**, 453-466.

63 H. J. Feng, T. R. Paudel, E. Y. Tsymbal and X. C. Zeng, *J. Am. Chem. Soc.*, 2015, **137**, 8227-8236.

64 W. Li, H. Dong, L. Wang, N. Li, X. Guo, J. Li and Y. Qiu, *J. Mater. Chem. A*, 2014, **2**, 13587-13592.

65 Y. Ogomi, A. Morita, S. Tsukamoto, T. Saitho, N. Fujikawa, Q. Shen, T. Toyoda, K. Yoshino, S. S. Pandey, T. Ma and S. Hayase, *J. Phys. Chem. Lett.*, 2014, **5**, 1004-1011.

66 P. W. Liang, C. C. Chueh, X. K. Xin, F. Zuo, S. T. Williams, C. Y. Liao and A. K. Y. Jen, *Adv. Energ. Mater.*, 2015, **5**, 1400960.

67 G. Giorgi, J. I. Fujisawa, H. Segawa and K. Yamashita, *J. Phys. Chem. Lett.*, 2013, **4**, 4213-4216.

68 K. Tanaka, T. Takahashi, T. Ban, T. Kondo, K. Uchida and N. Miura, *Solid State Commun.*, 2003, **127**, 619-623.

69 J. Feng and B. Xiao, *J. Phys. Chem. Lett.*, 2014, **5**, 1278-1282.